






# Updated Photon Scattering Coefficients ( $g$ \_values) for Mercury's Exospheric Species

Rosemary M. Killen<sup>1</sup> , Ronald J. Vervack Jr.<sup>2</sup> , and Matthew H. Burger<sup>3</sup> <sup>1</sup> NASA Goddard Space Flight Center, Planetary Magnetospheres Laboratory, Code 695, Greenbelt, MD 20771, USA; [rosemary.killen@nasa.gov](mailto:rosemary.killen@nasa.gov)<sup>2</sup> Johns Hopkins Applied Physics Laboratory, 11100 Johns Hopkins Rd., Laurel, MD 20723, USA<sup>3</sup> Space Telescope Science Institute, 3700 San Martin Dr., Baltimore, MD 21218, USA

Received 2022 August 24; revised 2022 October 2; accepted 2022 October 5; published 2022 December 7

## Abstract

In an optically thin exosphere such as those of Mercury and the Moon, the optically stimulated emissions are directly proportional to the stimulating solar flux. An important quantity in relating measured emission to column abundance in remote-sensing observations is the  $g$ \_value. The  $g$ \_value is proportional to the  $f$ -value of the emission line and to the solar flux at the emission frequency. The solar flux varies inversely with the heliocentric distance from the Sun, but also with the heliocentric relative velocity of the emitting atom. The heliocentric relative velocity of the planet Mercury varies by  $\pm 10 \text{ km s}^{-1}$ , however, the atoms may additionally have high velocities relative to the planet owing to high-energy processes or through acceleration caused by radiation pressure. In this paper we extend  $g$ \_values to heliocentric relative velocities  $\pm 50 \text{ km s}^{-1}$ . In addition to 12 species for which  $g$ \_values have been published previously, we have computed  $g$ \_values for two additional species, Mn and Al, that were discovered in Mercury's exosphere in the course of the MESSENGER mission. We have not included updated  $g$ \_values for C or OH, as these were not observed by MESSENGER. In this work, we employ the TSIS-1 hybrid reference solar spectrum for most calculations, with the SOLSTICE data being used in the EUV/far-UV. We note that the method employed here could be extended for application at extrasolar planets and comets, with the solar spectrum substituted by an appropriate stellar spectrum.

*Unified Astronomy Thesaurus concepts:* [Exosphere \(499\)](#); [Astronomy data modeling \(1859\)](#); [Ultraviolet spectroscopy \(2284\)](#); [Mercury \(planet\) \(1024\)](#)

*Supporting material:* data behind figures

## 1. Introduction

The discrete photoemission properties of atomic and molecular species stimulated by solar radiation are a valuable means of probing an atmosphere with remote-sensing experiments. In an optically thin atmosphere, the total column amount of a given species along the line of sight is dependent upon a solar-forced  $g$ \_value, defined as an emission probability per atom per incident photon ( $\text{photon s}^{-1} \text{ atom}^{-1}$ ). For an optically thin gas and a measured emission brightness,  $4\pi I$ , the column abundance,  $N$ , is obtained through the relation  $4\pi I = gN$ .

Mercury's exosphere is dominated by atomic emission at ultraviolet and visible wavelengths; thus,  $g$ \_values for the relevant species are needed for accurate retrieval of column densities from remote-sensing observations. Detected species of interest include sodium (Na), potassium (K), calcium (Ca), magnesium (Mg), manganese (Mn), aluminum (Al), hydrogen (H), helium (He), oxygen (O), and ionized calcium ( $\text{Ca}^+$ ), which have been observed from the ground, by Mariner 10 during its flybys, or by MESSENGER during its flybys and/or orbital phase. Additional species targeted by MESSENGER included sulfur (S) and ionized magnesium ( $\text{Mg}^+$ ), which have not yet been detected but for which analysis is ongoing. Many of these species will be targeted by BepiColombo during its flybys and orbital phase in the next few years; thus, the need for accurate  $g$ \_values.

The nature of the solar spectrum, including discrete emission in the EUV/far-UV (FUV) and Fraunhofer features at many wavelengths, introduces a strong dependence of the  $g$ \_values on Doppler velocity for many species. Because of Mercury's eccentric orbit (ellipticity of 0.2) and the subsequent variations in the solar flux with heliocentric distance, some  $g$ \_values can vary by over an order of magnitude during the orbital period. Furthermore,  $g$ \_values are dependent on the *instantaneous* heliocentric radial velocity of an atom, which varies not only as a function of Mercury's heliocentric radial velocity but also as a function of the atom's velocity as it is ejected from the surface and affected by gravitational and radiation-pressure accelerations along its trajectory.

In previous work (Killen et al. 2009a, 2009b),  $g$ \_values were calculated for 12 species that were to be targeted by the MESSENGER MASCS spectrometer. The range of relative velocities for which those  $g$ \_values were calculated was  $\pm 10 \text{ km s}^{-1}$ , the range of Mercury's heliocentric velocity relative to the Sun (Figure 1). However, the heliocentric relative velocities of atoms in Mercury's exosphere can vary considerably more than the velocity at rest with respect to the planet, owing to both the initial ejection velocity and the effects of gravity and radiation pressure. This motivates the work here, which extends the calculations of Killen et al. (2009a, 2009b) to larger velocities and considers a more uniform treatment of the solar spectrum. Although calculated for application to Mercury's exosphere, these quantities are also applicable to other astronomical observations where emission is forced by solar radiation. All  $g$ \_values can be scaled to the appropriate heliocentric distance by the inverse square of the heliocentric distance.



Original content from this work may be used under the terms of the [Creative Commons Attribution 4.0 licence](#). Any further distribution of this work must maintain attribution to the author(s) and the title of the work, journal citation and DOI.

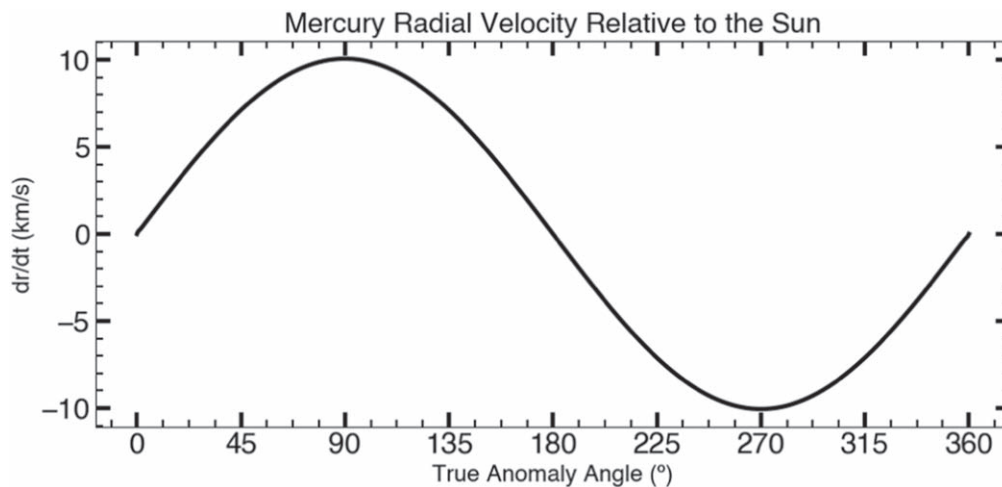


Figure 1. Mercury’s radial velocity relative to the Sun as a function of Mercury’s true anomaly angle.

## 2. Method

The volumetric excitation rate  $g_{ij}$  of state  $j$  is proportional to the solar flux at the frequency  $\nu$  and absorption coefficient of the transition  $i-j$ .

If the solar flux is in photons  $\text{cm}^{-2} \text{s}^{-1} \text{\AA}^{-1}$  then

$$g_{ij} = \pi F_{\lambda} (\lambda^2/c) (\pi e^2/mc) f_{ij} \quad (1)$$

where  $\pi F_{\lambda}$  is in photon  $\text{cm}^{-2} \text{s}^{-1} \text{\AA}^{-1}$  at heliocentric distance,  $r$ ,  $\lambda^2$  is  $\lambda(\text{\AA}) \cdot \lambda(\text{cm})$ ,  $c$  is in  $\text{cm s}^{-1}$ ,  $(\pi e^2)/(mc)$  is the integrated absorption coefficient per atom for unit  $f$ -value, in  $\text{cm}^2 \text{s}^{-1}$ , and  $f_{ij}$ , the oscillator strength, or  $f$ -value, is related to the transition probability. The  $f$ -values were obtained from the NIST database (Kramida et al. 2021). We assume herein that the atoms are cold, thus they initially reside in the ground state. This is appropriate for a collisionless medium. The absorption coefficient does not change, but the solar flux at Mercury at the rest frequency of the transition varies with Mercury’s Doppler shift. Therefore, the only variable of interest is the instantaneous solar flux seen at Mercury by the atom, which in turn is a function of Mercury’s radial velocity relative to the Sun and the velocity of the atom as ejected and affected by gravity and radiation pressure. Radiation pressure is especially strong for Na and K and can accelerate atoms to high velocity down the tail antisunward of Mercury. The velocity of Ca atoms is also extreme (e.g., Burger et al. 2012, 2014), owing to as yet unknown processes but possibly due to dissociation of a Ca-bearing molecule (Killen et al. 2005), and velocities of other refractory species may be high at times as well (Merkel et al. 2017). We have therefore extended the  $g$ -values to  $\pm 50 \text{ km s}^{-1}$  relative to their at-rest values to facilitate analyses of observations of Mercury’s exosphere.

The physical considerations involved in the calculation of photon scattering probabilities are discussed by Mitchell & Zemansky (1971, Chapters 3, 5). Chamberlain (1961, p. 424) provides a definition of  $g$ -value, but the formulation is not general and does not account for radiationless deactivation, the distribution of the population in states of the excited species, or the kinetic temperature of the fluorescent volume. The calculations presented in Killen et al. (2009a, 2009b)

intrinsically included all of the latter effects. Those model calculations, however, assumed isotropic scattering, and did not address polarization effects or the scattering phase function as discussed by Chamberlain (1961, Section 11.1.2) and Mitchell & Zemansky (1971, Chapter 5).

Each atom absorbs at the discrete frequency of its atomic line. Accurate calculations must therefore be made at the instantaneous velocity of the atom using a high-resolution solar spectrum. The solar spectra employed in this work came from several different sources, depending on the wavelength region. To ensure that the  $g$ -values for all species are representative of the same general solar conditions, we chose dates that correspond to solar minimum conditions in all cases. Note that the solar spectra shown in Figures 2–16 have not been scaled to the 0.352 au heliocentric distance at which the  $g$ -values are calculated but are relative to 1 au so that comparisons of the spectra used to other reference spectra are more easily facilitated. The irradiance units on all the solar spectra are  $\text{W m}^{-2} \text{\AA}^{-1}$  with the exception of the spectrum for H Ly $\alpha$ , which is in units of photons  $\text{cm}^{-2} \text{s}^{-1} \text{\AA}^{-1}$  owing to its origin (see below). All wavelengths are in angstroms.

For all species with emission lines at wavelengths greater than 2000  $\text{\AA}$ , the TSIS-1 Hybrid Solar Reference Spectrum (Coddington et al. 2021) was used, as this is the accepted standard for that wavelength range. The spectral data were obtained from the LASP LISIRD website,<sup>4</sup> (Leise et al. 2021). No specific date was chosen as the TSIS-1 spectrum is an average spectrum for conditions during the solar minimum between solar cycles 24 and 25. The EUV lines are influenced by variations in the solar spectrum (e.g., Snow et al. 2005), thus those  $g$ -values, particularly for H, He, O, S, and  $\text{Mg}^+$ , should be scaled to the solar flux at the time of the observations as well as to the heliocentric distance.

For the sulfur triplet lines between 1807 and 1826  $\text{\AA}$ , the SORCE SOLSTICE high-resolution solar spectral irradiance was used, with the date corresponding to 2009 March 1 (prior to the power-cycling issues that began in 2010). The spectral data were obtained from the LASP LISIRD website.

For the oxygen triplet lines between 1302 and 1306  $\text{\AA}$ , we generated line-shape profiles according to Gladstone (1992) and

<sup>4</sup> <https://lasp.colorado.edu/lisird/>

then scaled them to the appropriate irradiance levels in the same SORCE SOLSTICE spectrum used for the sulfur triplet lines.

For the He 584 Å line, we used the theoretical line-shape profile of Golding et al. (2017; their Figure 10) and scaled the irradiance to the TIMED SEE solar spectral irradiance Level 3A for 2009 March 1. The spectral data were downloaded from the LASP LISIRD site.

For the H Ly $\alpha$  line, we used the line profile observed by SUMER/SOHO (Lemaire et al. 2015; their Figure 5(b)) for 2009 April 16. The spectral data were downloaded from the CDS website provided in the referenced paper.

### 3. Results

This section presents the updated  $g$ -values for various species of importance to Mercury’s exosphere. All  $g$ -values shown are calculated for a Mercury heliocentric distance of 0.352 au, but may be easily scaled to other heliocentric distances. Figures are shown in the main text; data are available as ASCII files through the online-only materials.

#### 3.1. Sodium

Updated  $g$ -values for the Na D<sub>1</sub> (5897.56 Å) and D<sub>2</sub> (5891.58 Å) lines are shown in Figure 2. Sodium atoms are particularly affected by radiation pressure, which is highly variable with the true anomaly angle (TAA) of the planet (e.g., Smyth & Marconi 1995). Because of feedbacks between the positive or negative velocity of Mercury with respect to the Sun and radiation-pressure acceleration, which is always antisunward, the acceleration is greatest on the outbound leg of the orbit (TAA < 180°) (Potter et al. 2007). It can be seen in Figure 2 that the Na  $g$ -values increase more than a factor of 2 from  $v_{\text{rel}} = \pm 10 \text{ km s}^{-1}$  to  $v_{\text{rel}} = \pm 50 \text{ km s}^{-1}$ . The variation is fairly symmetric but has some structure due to the underlying solar spectrum.

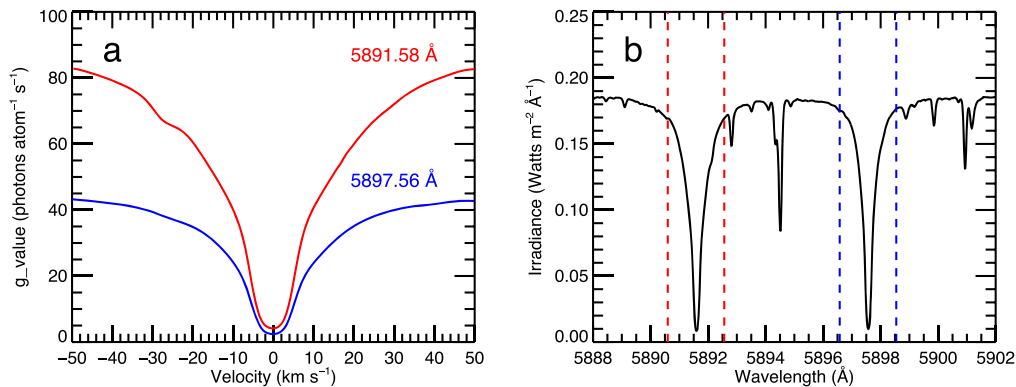


**Figure 2.** (a) Updated  $g$ -values for the Na D<sub>2</sub> (5891.58 Å) and D<sub>1</sub> (5897.56 Å) lines and (b) the solar spectrum in the region of the lines. The dashed lines in (b) indicate the range of wavelengths corresponding to the  $g$ -values shown in (a). The TSIS-1 reference spectrum was used for Na.

(The data used to create this figure are available.)

#### 3.2. Calcium

Updated Ca  $g$ -values are shown in Figure 3 for the 4227.92 Å line, the most common Ca line observed with ground-based telescopes, as well as from space-borne instruments. Radiation pressure is not important for Ca at Mercury owing to rapid photoionization (see Huebner & Mukherjee 2015). However, Ca atoms in Mercury’s exosphere are highly energetic and have been shown to have extreme velocity with respect to the planet, and thus with respect to the Sun (Burger et al. 2014). Doppler shifts of the lines are therefore much different than they would be if calculated at rest with respect to the planet.

In the case of calcium, the  $g$ -value is not symmetric for the inbound and outbound legs of the orbit. For the outbound portion (positive heliocentric relative velocity), the  $g$ -value continues to increase as the atom is accelerated antisunward, except for a small decrease between 20 and 25 km s<sup>-1</sup>. This provides a positive feedback as the atom is accelerated by radiation pressure. On the inbound leg, the  $g$ -value is not symmetric. For relative velocities between  $-35$  and  $-50 \text{ km s}^{-1}$  the  $g$ -value decreases as the atom is accelerated antisunward. If the atom initially has a negative heliocentric relative velocity greater than  $|35| \text{ km s}^{-1}$  (i.e., between  $-50$  and  $-35 \text{ km s}^{-1}$  on this figure) there will be a positive feedback with acceleration, but for relative velocities between  $-35$  and  $0 \text{ km s}^{-1}$  there is a negative feedback with acceleration. Given the short photoionization lifetime, however, radiation pressure is not important for Ca and large negative heliocentric velocities are unlikely.

#### 3.3. Magnesium

Updated  $g$ -values for the Mg line at 2852.96 Å are shown in Figure 4. The  $g$ -values between  $-10$  and  $10 \text{ km s}^{-1}$  differ significantly from those published by Killen et al. (2009a, 2009b). In part this is related to the spectrum utilized by Killen et al. having a higher-resolution solar spectrum than the TSIS-1 reference spectrum used here (15 mÅ versus 250 mÅ). However, the Killen et al. spectrum also exhibited

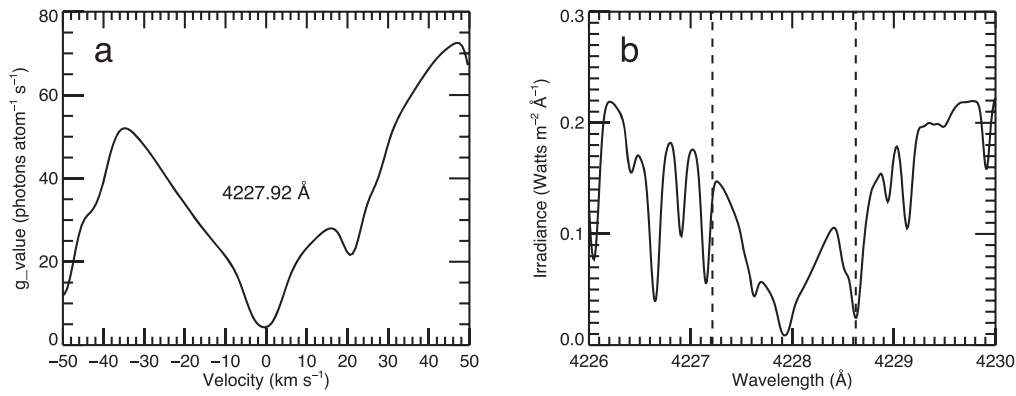


**Figure 3.** (a) Updated  $g$ \_values for the Ca 4227.92 Å line and (b) the solar spectrum in the region of the line. The dashed lines in (b) indicate the range of wavelengths corresponding to the  $g$ \_values shown in (a). The TSIS-1 reference spectrum was used for Ca. (The data used to create this figure are available.)

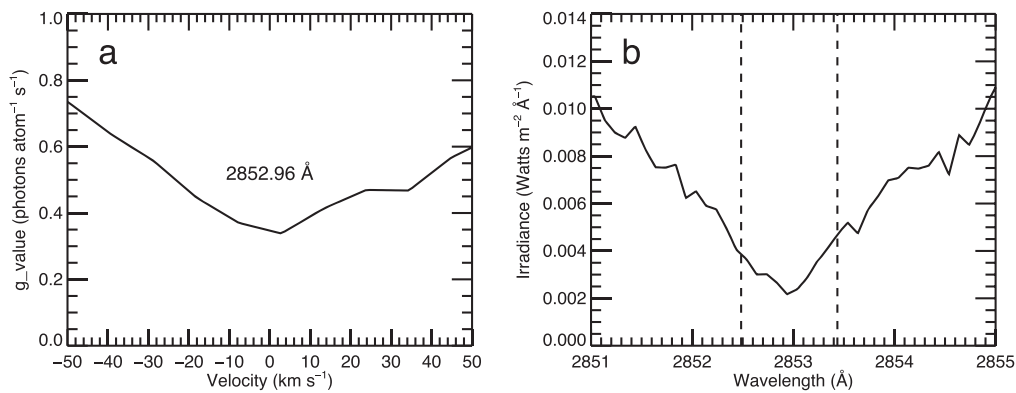


**Figure 4.** (a) Updated  $g$ \_values for the Mg 2852.96 Å line and (b) the solar spectrum in the region of the line. The dashed lines in (b) indicate the range of wavelengths corresponding to the  $g$ \_values shown in (a). The TSIS-1 reference spectrum was used for Mg. (The data used to create this figure are available.)

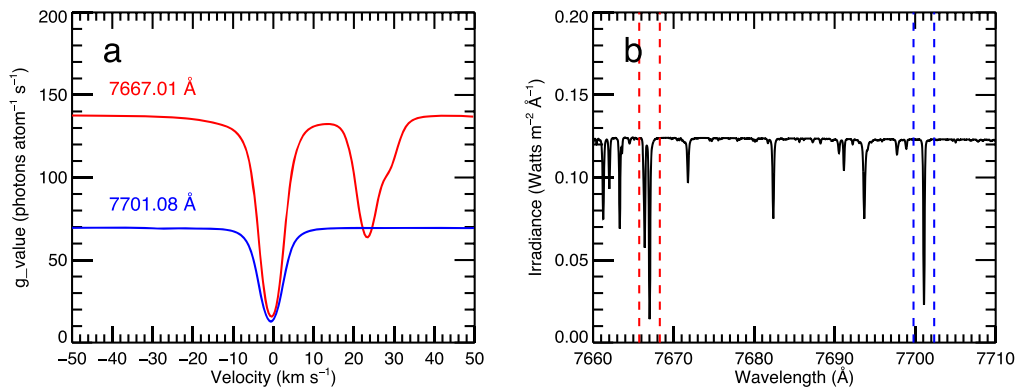


**Figure 5.** (a) Updated  $g$ \_values for the visible K ( $D_1$ ) line at 7701.08 Å and K ( $D_2$ ) at 7667.01 Å and (b) the solar spectrum in the region of the lines. The dashed lines in (b) indicate the range of wavelengths corresponding to the  $g$ \_values shown in (a). The TSIS-1 reference spectrum was used for K at these wavelengths. (The data used to create this figure are available.)

emission lines within the relevant wavelength region (Figure 4(b)) that are not present in the TSIS-1 spectrum.

Although the Killen et al. (2009a, 2009b) spectrum was ostensibly a spectrum from Hall & Anderson (1991), we have not been able to confirm its origin. We are not aware of any

solar lines at the relevant wavelengths where these emission lines appear in the Killen et al. spectrum, although it is possible that there may be some that are sporadic. It is also possible that the Killen et al. spectrum could include lines from meteor ablation. If the line in Killen et al. that appears at 2852.87 Å is a

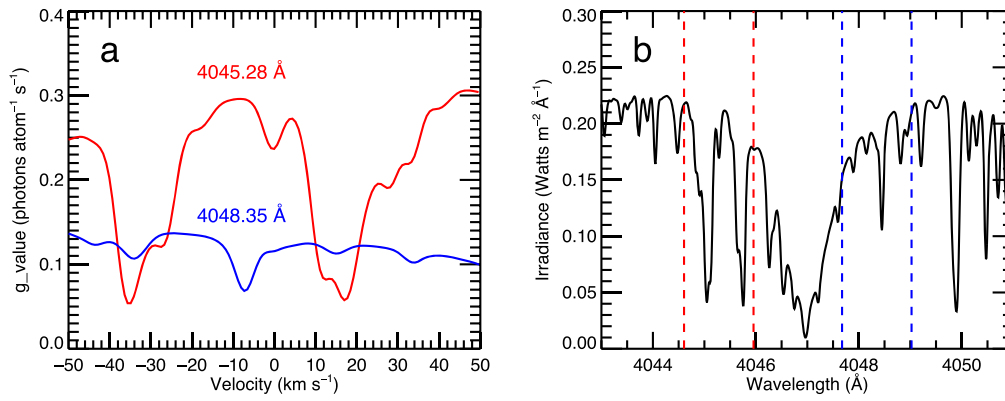


**Figure 6.** (a) Updated  $g$ \_values for K 4045.24 Å and 4048.36 Å and (b) the solar spectrum in the region of the lines. The dashed lines in (b) indicate the range of wavelengths corresponding to the  $g$ \_values shown in (a). The TSIS-1 reference spectrum was used for K at these wavelengths.

(The data used to create this figure are available.)

Doppler-shifted Mg I line, then the Doppler shift is  $-9 \text{ km s}^{-1}$ . However, if this were a meteor ablation line, then emission lines from Cu, Fe, K, Cr, Na, Li, and Rb would most likely also be present and most likely would be from the ions. Additional ultra-high-resolution solar spectra are needed to resolve these discrepancies, as the presence of these lines in the solar spectrum can significantly change the  $g$ \_values.

The  $g$ \_values derived with the TSIS-1 spectrum are slightly asymmetric with respect to the positive and negative  $v_{\text{rel}}$ , but they are not as asymmetric nor as strongly varying as in Killen et al. (2009a, 2009b). The resulting  $g$ \_values are uniformly lower than those from Killen et al. as well. In general, derived column abundances will be higher by factors of 2–4 using the updated  $g$ \_values, which has implications for analyses that have utilized the Killen et al.  $g$ \_values. The difference and the consequences for the Mg exosphere have been discussed in Chaufray et al. (2022). The implications for exospheric studies emphasize the need for higher-spectral-resolution solar spectra.

### 3.4. Potassium

Potassium can be observed in the visible at 7667.01 and 7701.08 Å, and updated  $g$ \_values for these lines are shown in

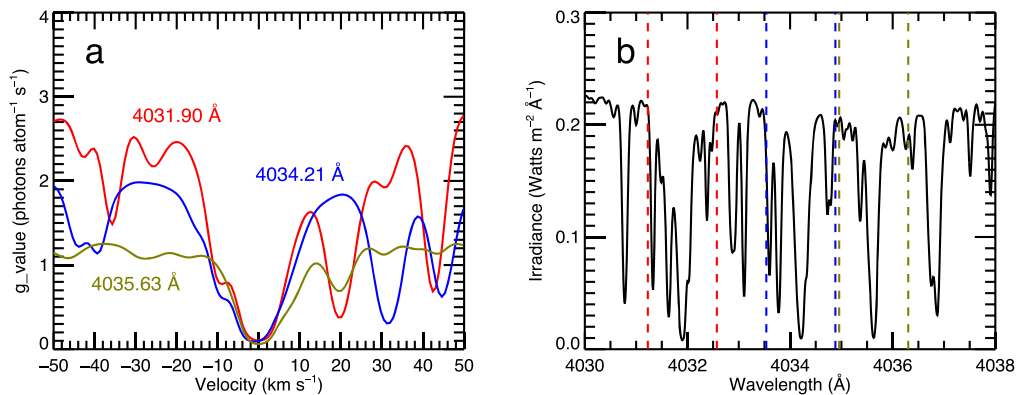


**Figure 7.** (a) Updated  $g$ \_values for the Mn lines at 4031.21 Å, 4034.21 Å, and 4035.63 Å and (b) the solar spectrum utilized in the region of the lines. The dashed lines in (b) indicate the range of wavelengths corresponding to the  $g$ \_values shown in (a). The TSIS-1 reference spectrum was used for Mn. This region of the spectrum is crowded with solar features that complicate the  $g$ \_values.

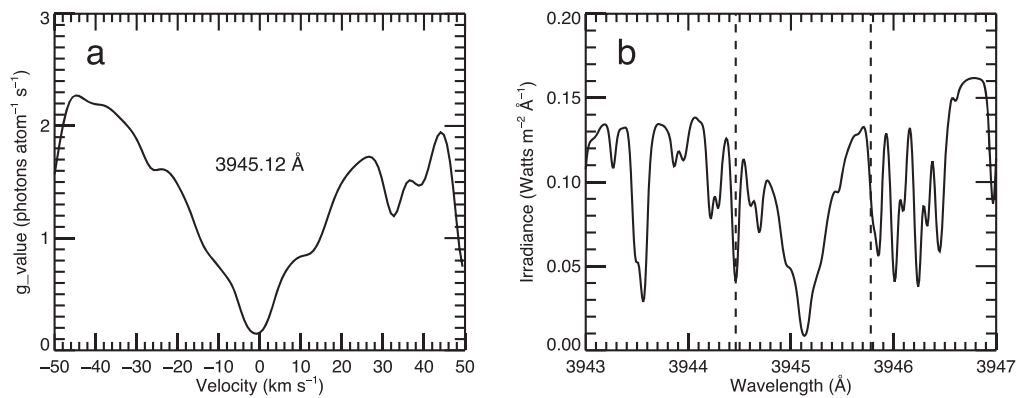
(The data used to create this figure are available.)

Figure 5. Although there is little variation in the K  $D_1$  line beyond the core of the line, there is an additional solar line that causes variation in the K  $D_2$  line for positive heliocentric relative velocities between  $+20$  and  $30 \text{ km s}^{-1}$  (Figure 5(a)).

Updated  $g$ \_values for the K lines at 4045.28 Å ( $D_2$ ) and 4048.35 Å ( $D_1$ ) are shown in Figure 6. These K lines are within the ranges of the MESSENGER and BepiColombo instruments, and primarily reflect the underlying solar spectrum. Most notably, deep Fraunhofer lines on either side of the K( $D_2$ ) line cause a steep decline in the K( $D_2$ )  $g$ \_value at high Doppler shift. As the  $g$ \_value declines for radiation-pressure-accelerated atoms in the tail, the K abundance can be strongly underestimated if  $g$ \_values for a lower radial velocity are used.

### 3.5. Manganese

Mn was discovered in Mercury’s exosphere in the final Earth year of the MESSENGER mission by the MASCS UV spectrometer (Vervack et al. 2016). It is believed to occur sporadically in Mercury’s exosphere. The Mn triplet may be unresolved in the PHEBUS spectrometer on board BepiColombo (Quemerais et al. 2020).



**Figure 8.** (a) Updated  $g$ -values for the Al line at 3945.12 Å and (b) the solar spectrum utilized in the region of the lines. The dashed lines in (b) indicate the range of wavelengths corresponding to the  $g$ -values shown in (a). The TSIS-1 reference spectrum was used for Al.

(The data used to create this figure are available.)

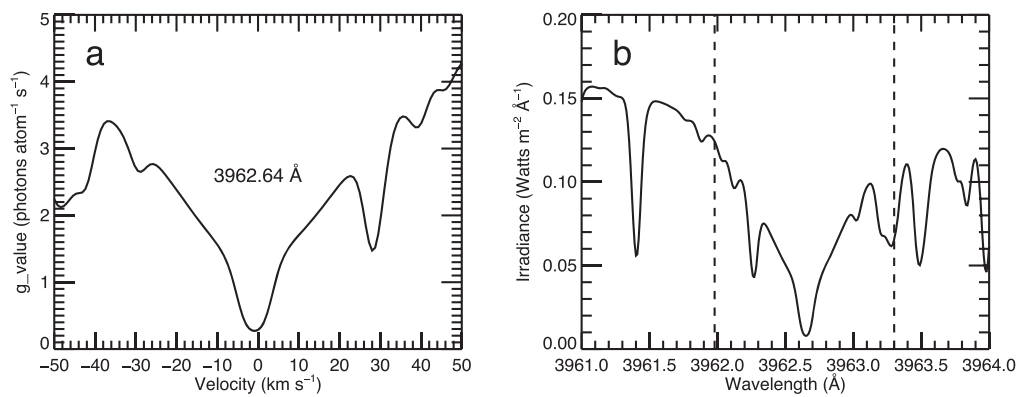


**Figure 9.** (a) Updated  $g$ -values for the Al line at 3962.64 Å and (b) the solar spectrum utilized in the region of the lines. The dashed lines in (b) indicate the range of wavelengths corresponding to the  $g$ -values shown in (a). The TSIS-1 reference spectrum was used for Al.

(The data used to create this figure are available.)

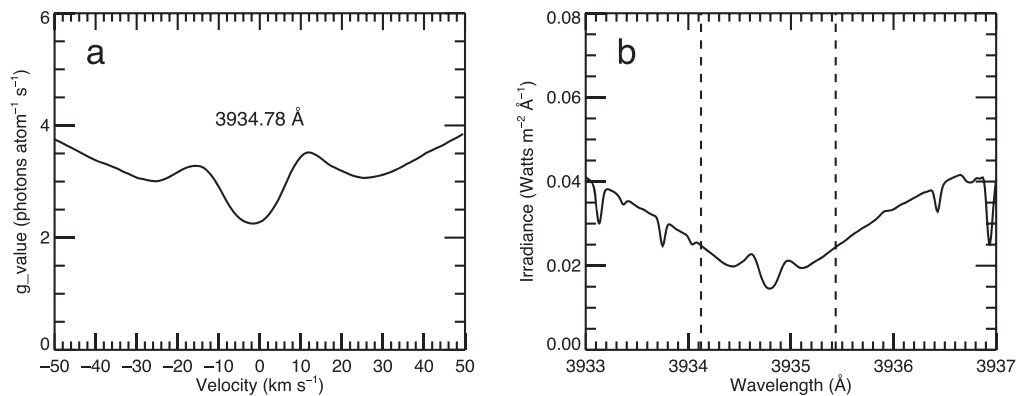


**Figure 10.** (a) Updated  $g$ -values for Ca $^{+}$  at 3934.78 Å lines and (b) the solar spectrum utilized in the region of the line. The dashed lines in (b) indicate the range of wavelengths corresponding to the  $g$ -values shown in (a). The TSIS-1 reference spectrum was used for Ca $^{+}$ .

(The data used to create this figure are available.)

### 3.6. Aluminum

Aluminum was first discovered in Mercury's exosphere in observations taken with the Keck I HIRES spectrograph (Bida & Killen 2017) and subsequently was observed in the last year of MESSENGER's mission (Vervack et al. 2016). Updated

$g$ -values for the Al lines at 3945.12 Å (D $_1$ ) and 3962.64 Å (D $_2$ ) are shown in Figures 8 and 9, respectively. These Al lines are within the ranges of the MESSENGER and BepiColombo instruments, and primarily reflect the underlying solar spectrum. Most notably, a deep Fraunhofer line affects the  $g$ -value for Al 3963 between +20 and 30 km s $^{-1}$  line. The  $g$ -value for

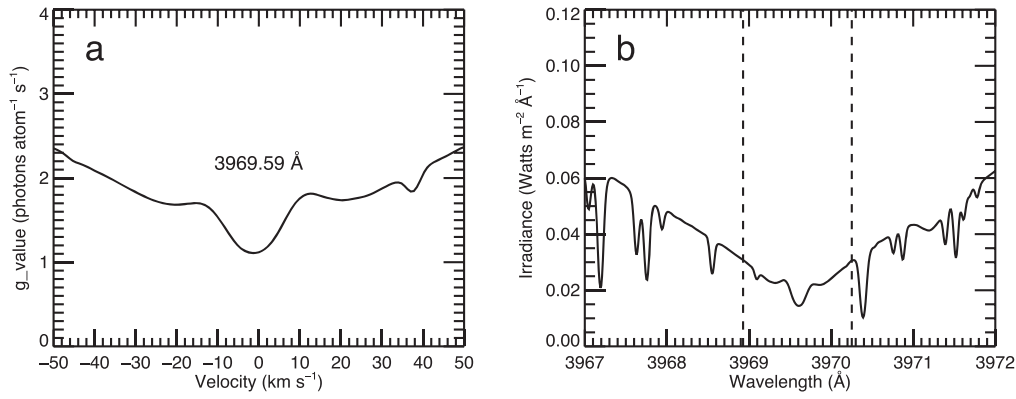


**Figure 11.** (a) Updated  $g$ -values for  $\text{Ca}^+$  at 3969.59 Å lines and (b) the solar spectrum utilized in the region of the line. The dashed lines in (b) indicate the range of wavelengths corresponding to the  $g$ -values shown in (a). The TSIS-1 reference spectrum was used for  $\text{Ca}^+$ .

(The data used to create this figure are available.)

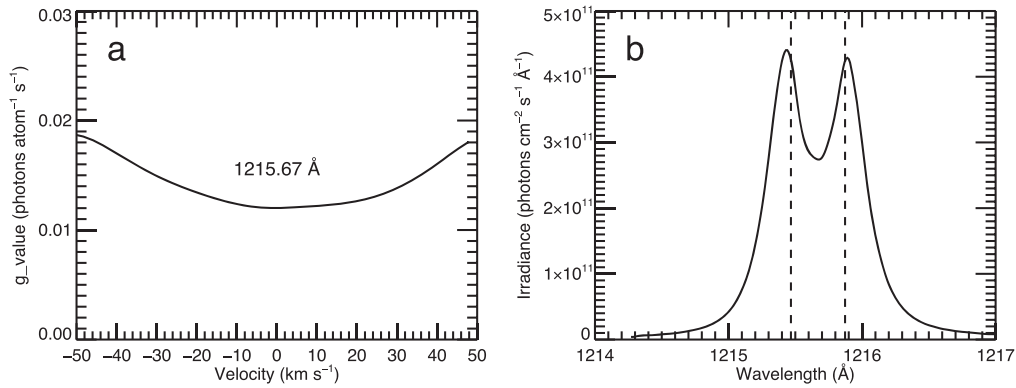


**Figure 12.** (a) Updated  $g$ -values for the combined H Ly $\alpha$  lines at 1215.668 and 1215.67 Å and (b) the solar spectrum utilized in the region of the lines. The dashed lines in (b) indicate the range of wavelengths corresponding to the  $g$ -values shown in (a). For the H Ly $\alpha$  line, we used the line profile observed by SUMER/SOHO (Lemaire et al. 2015; their Figure 5(b)) for 2009 April 16. The spectral data were downloaded from the CDS website provided in the referenced paper.

(The data used to create this figure are available.)

the 3945 Å line is highly asymmetric for  $|v| > 20 \text{ km s}^{-1}$ . For higher heliocentric radial velocities, the Al abundance would be underestimated if  $g$ -values for a radial velocity between  $\pm 10 \text{ km s}^{-1}$  are used.

### 3.7. Ionized Calcium

Updated  $g$ -values for  $\text{Ca}^+$  lines at 3934.78 and 3969.59 Å are shown in Figures 10 and 11. There is structure in the  $g$ -values for both lines. The  $g$ -values increase slightly to either side of zero velocity, then decrease slightly before ultimately increasing out to the velocity limits calculated here, with only a small variation in the  $g$ -values for the 3969.59 Å line owing to a solar feature.

### 3.8. Hydrogen

Updated  $g$ -values for the H Ly $\alpha$  lines near 1216 Å are shown in Figure 12. Even though the Ly $\alpha$  solar line is in emission, there is considerable self-absorption in the line center, causing the line as seen at Mercury to appear in absorption rather than in emission. The  $g$ -values for the two H Ly $\alpha$  lines continue to increase as heliocentric velocities

increase to  $\pm 50 \text{ km s}^{-1}$ , which results in a decrease in derived H abundances with higher relative velocities.

### 3.9. Helium

Updated  $g$ -values for the He 584.33 Å line are shown in Figure 13. The  $g$ -value continues to decrease as heliocentric velocities increase beyond that calculated in Killen et al. (2009a, 2009b). Correspondingly, calculated column abundances will increase if the atom's heliocentric relative velocity is large. This is not expected to be the case at Mercury because radiation pressure will be small for these wavelengths and the helium atoms are expected to be thermally desorbed for the most part. There is an asymmetry between positive and negative velocities where the  $g$ -value turns down near  $+11 \text{ km s}^{-1}$  or  $-19 \text{ km s}^{-1}$ .

### 3.10. Oxygen

Updated  $g$ -values for the O triplet near 1304 Å are shown in Figure 14. Considerable error in the estimation of densities can occur if the heliocentric relative velocity of an oxygen atom is not correctly considered. The  $g$ -value for O I (1302 Å) shows a steady increase away from the local minimum near  $-3 \text{ km s}^{-1}$

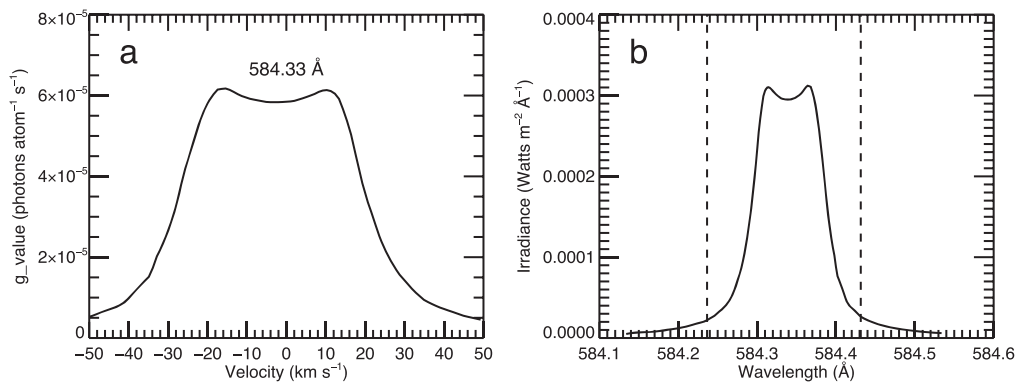


**Figure 13.** (a) Updated  $g$ -values for the He 584.33 Å line and (b) the solar spectrum utilized in the region of the line. The dashed lines in (b) indicate the range of wavelengths corresponding to the  $g$ -values shown in (a). For the He 584 Å line, we used the theoretical line-shape profile of Golding et al. (2017; their Figure 10) and scaled the irradiance to the TIMED SEE solar spectral irradiance Level 3A for 2009 March 1. The spectral data were downloaded from the LASP LISIRD site. (The data used to create this figure are available.)

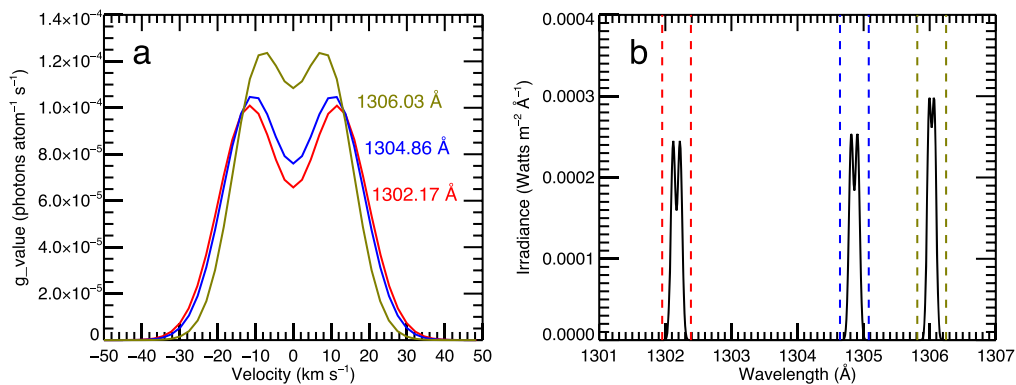


**Figure 14.** (a) Updated  $g$ -values for the three FUV O I lines at 1302.17, 1304.86, and 1306.03 Å, respectively, and (b) the solar spectrum utilized in the region of the lines. The dashed lines in (b) indicate the range of wavelengths corresponding to the  $g$ -values shown in (a). For the oxygen triplet lines between 1302 and 1306 Å, we generated line-shape profiles according to Gladstone (1992) and then scaled them to the appropriate irradiance levels in the same SOLAR SOLSTICE spectrum used for the sulfur triplet lines. (The data used to create this figure are available.)

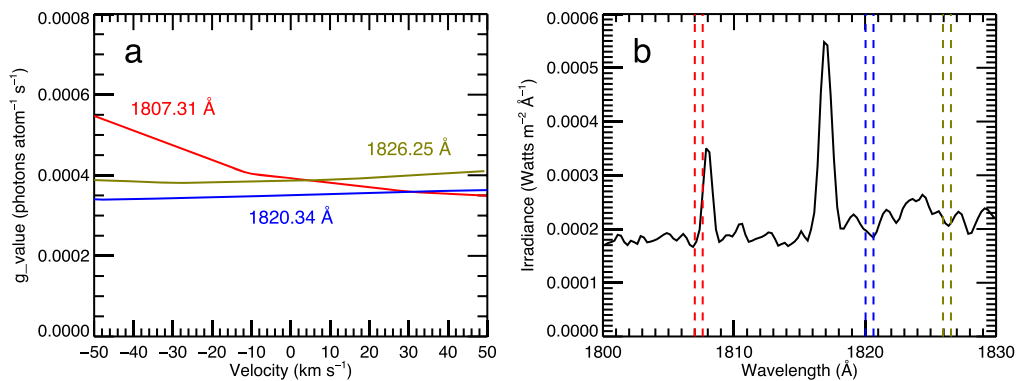


**Figure 15.** (a) Updated  $g$ -values for the three S I lines at 1807.31, 1820.34, and 1826.25 Å and (b) the solar spectrum utilized in the region of the lines. The dashed lines in (b) indicate the range of wavelengths corresponding to the  $g$ -values shown in (a). The SOLAR SOLSTICE high-resolution spectrum was used for S, with the date corresponding to 2009 March 1 (prior to the power-cycling issues that began in 2010). The spectral data were obtained from the LASP LISIRD website. (The data used to create this figure are available.)



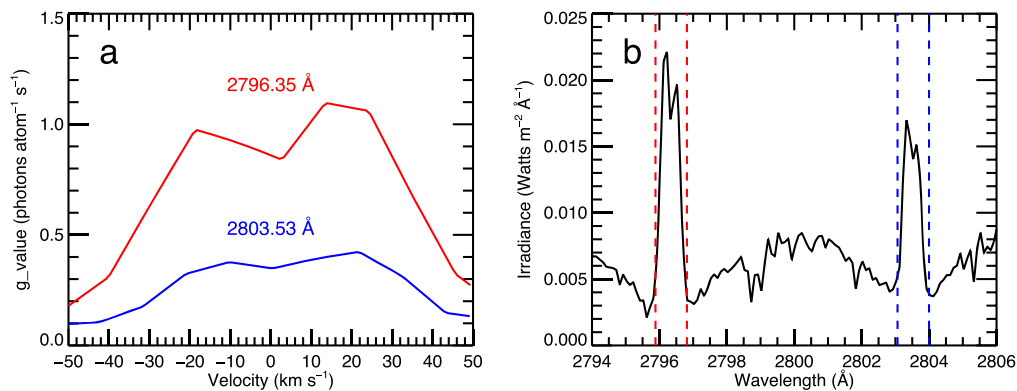


**Figure 16.** (a) Updated  $g$ \_values for  $\text{Mg}^+$  lines at 2796.35 Å and 2803.53 Å and (b) the solar spectrum utilized in the region of the lines. The dashed lines in (b) indicate the range of wavelengths corresponding to the  $g$ \_values shown in (a). The TSIS-1 reference spectrum was used for  $\text{Mg}^+$ . (The data used to create this figure are available.)

but decreases for  $v < -20 \text{ km s}^{-1}$  or  $v > 10 \text{ km s}^{-1}$ . For large positive or negative heliocentric relative velocities, the oxygen abundance can be severely underestimated with static  $g$ \_values.

### 3.11. Sulfur

Updated  $g$ \_values for the S triplet between 1807–1826 Å are shown in Figure 15. The solar spectrum in the FUV does not have sufficient resolution to show whether the  $g$ \_values are smooth or not. The  $g$ \_value shown here shows discrete jumps due solely to the resolution of the underlying solar spectrum used in the calculations. If the column abundance of S is  $10^{12} \text{ atoms cm}^{-2}$ , the maximum emission expected is about 200 R, which would have been observable with the MASCs UV spectrometer on MESSENGER but which has not been detected (unpublished results). The BepiColombo PHEBUS UV spectrometer (Quemerais et al. 2020) will also have a chance to detect S at these wavelengths if the abundances are high enough, as lower column abundances are likely too difficult to detect.

### 3.12. Ionized Magnesium

Updated  $g$ \_values for  $\text{Mg}^+$  lines at 2796.35 Å and 2803.53 Å are shown in Figure 16. The  $g$ \_values for both lines are mostly related to emission features in the solar spectrum at the cores of the solar Fraunhofer features and thus have a similar structure to  $g$ \_values for the EUV and FUV lines. The FIPS instrument on board MESSENGER measured ions with energies from 0.046 to 13.3 keV, thus velocities ranging from 1 to 322  $\text{km s}^{-1}$ . Newly created ions from the exosphere would be close to the low end of the velocity range with a few tens of eVs of energy.

## 4. Conclusions

We have presented  $g$ \_values calculated to  $\pm 50 \text{ km s}^{-1}$  heliocentric relative velocity for species previously observed from the ground, by Mariner 10, or by MESSENGER MASCs or at least attempted (in the case of MESSENGER). Most of these lines are expected to be targeted by the PHEBUS spectrometer on board BepiColombo. Because some atoms in Mercury’s exosphere have been shown to have large heliocentric relative velocities, these updated  $g$ \_values compared to those presented in Killen et al. (2009a, 2009b) are of

great importance when modeling exospheric emissions at Mercury, and especially when comparing with observations.

As an example, the Monte Carlo code developed by Burger et al. (2010, 2012, 2014), used to model the exosphere of Mercury for comparison to observed emission from MESSENGER MASCs (e.g., Killen et al. 2022), saves the velocity of the atom at each time step. The instantaneous  $g$ \_value is used in this model code to calculate the emission and radiation pressure of each atom (or packet of atoms) at each time step. After calculation of the aggregate emissions at high spectral resolution, the emission must be convolved with the instrument function and integrated over the line of sight and the instrument cone angle to compare the calculated emission with the observed emission. All  $g$ \_values must be employed at the *instantaneous* atomic velocity of *each* atom and at the highest spectral resolution possible for the determination of column density from observed emission to be accurate.

The results presented in this article rely in part on data from the LASP Interactive Solar Irradiance Datacenter (LISIRD) (<https://lasp.colorado.edu/lisird/>). R.J.V., R.M.K., and M.H.B. acknowledge funding from NASA DDAP grant 80NSSC18K0352. R.M.K. and M.H.B. acknowledge funding from the NASA solar system Workings program award Nos. 80NSSC18K0521 and 80NSSC22K0099. R.J.V. and R.M.K. acknowledge funding from the NASA SSO grant 80NSSC18K0857. R.M.K. was partially supported by the GSFC ISFM and from STROFIO, a NASA-funded mass spectrometer on board BepiColombo.

### ORCID iDs

Rosemary M. Killen  <https://orcid.org/0000-0002-0543-2326>

Ronald J. Vervack Jr.  <https://orcid.org/0000-0002-8227-9564>

Matthew H. Burger  <https://orcid.org/0000-0002-9334-7198>

### References

- Bida, T. A., & Killen, R. M. 2017, *Icar*, 289, 227  
 Burger, M., Killen, R. M., Vervack, R. J., Jr., et al. 2010, *Icar*, 209, 63  
 Burger, M. H., Killen, R. M., McClintock, W. E., et al. 2012, *JGRE*, 117, E00L11  
 Burger, M. H., Killen, R. M., McClintock, W. E., et al. 2014, *Icar*, 238, 51  
 Chamberlain, J. W. 1961, *Physics of the Aurora and Airglow* (New York: Academic Press)

- Chaufray, J.-Y., Leblanc, F., Werner, A. I. E., Modolo, R., & Aizawa, S. 2022, *Icar*, **384**, 115081
- Coddington, O. M., Richard, E. C., Harber, D., et al. 2021, *GeoRL*, **48**, e2020GL091709
- Gladstone, G. R. 1992, *JGR*, **97**, 19519
- Golding, T. P., Leenaarts, J., & Carlsson, M. 2017, *A&A*, **597**, A102
- Hall, L. A., & Anderson, G. P. 1991, *JGR*, **96**, 12927
- Huebner, W. F., & Mukherjee, J. 2015, *P&SS*, **106**, 11
- Killen, R. M., Morrissey, L. S., Burger, M. H., et al. 2022, *PSJ*, **3**, 139
- Killen, R. M. D. E., Shemansky, & Mouawad, N. 2009a, *ApJS*, **181**, 351
- Killen, R. M. D. E., Shemansky, & Mouawad, N. 2009b, *ApJS*, **182**, 667
- Killen, R. M., Bida, T., & Morgan, T. H. 2005, *Icar*, **173**, 300
- Kramida, A., Ralchenko, Yu., Reader, J. & NIST ASD Team 2021, NIST Atomic Spectra Database, v5.9 (Gaithersburg, MD: National Institute of Standards and Technology), <https://physics.nist.gov/asd>
- Leise, H., Lindholm, D. M., Lindholm, C., et al. 2021, AGU Fall Meeting 2021 (Washington, DC: American Geophysical Union), SH55A–1822
- Lemaire, P., Vial, J.-C., Curdt, W., Schuhle, U., & Wilhelm, K. 2015, *A&A*, **581**, A26
- Merkel, A. W., Timothy, A., & Cassidy, R. J. 2017, *Icar*, **281**, 46
- Mitchell, A. C. G., & Zemansky, M. W. 1971, *Resonance Radiation and Excited Atoms* (Cambridge: Cambridge Univ. Press)
- Potter, A. E., Killen, R. M., & Morgan, T. H. 2007, *Icar*, **186**, 571
- Quemerais, E., Chaufray, J.-Y., Koutroumpa, D., Leblanc, F., et al. 2020, *SSRv*, **216**, 67
- Smyth, W. H., & Marconi, M. L. 1995, *ApJ*, **441**, 839
- Snow, M., Woods, T. N., Eparvier, F. G., et al. 2005, AGU Fall Meeting 2005 (Washington, DC: American Geophysical Union), IN33B–1180
- Vervack, R. J., Jr., Killen, R. M., McClintock, W. E., et al. 2016, *GeoRL*, **43**, 11545